ADVANCING EARTH AND SPACE SCIENCE

Earth and Space Science

METHOD

10.1029/2022EA002537

Detecting Discontinuities From In Situ Space Measurements: Method and FPGA Implementation

C. Munteanu[1], D. C. Turicu[2], O. Creţ[2], and M. Echim[1,3]

[1]Institute of Space Science, Măgurele, Romania, [2]Technical University of Cluj-Napoca, Cluj-Napoca, Romania, [3]Royal Belgian Institute for Space Aeronomy, Brussels, Belgium

Key Points:

- We designed an algorithm to detect directional discontinuities from in-situ space measurements, suitable for automated application
- A Field-Programmable Gate Array (FPGA) implementation of the algorithm, designed to be adapted for on-board operations, is provided
- Tests with laboratory and space measurements of the FPGA and software implementations of the detection algorithm give excellent results

Correspondence to:

D. C. Turicu,
dan.turicu@cs.utcluj.ro

Citation:

Munteanu, C., Turicu, D. C., Creţ, O., & Echim, M. (2022). Detecting discontinuities from in situ space measurements: Method and FPGA implementation. *Earth and Space Science*, *9*, e2022EA002537. https://doi.org/10.1029/2022EA002537

Received 26 JUL 2022
Accepted 29 SEP 2022

Author Contributions:

Conceptualization: C. Munteanu, D. C. Turicu, O. Creţ, M. Echim
Formal analysis: C. Munteanu, D. C. Turicu
Funding acquisition: O. Creţ, M. Echim
Methodology: C. Munteanu, D. C. Turicu, O. Creţ, M. Echim
Software: C. Munteanu, D. C. Turicu
Supervision: O. Creţ, M. Echim
Validation: C. Munteanu, D. C. Turicu
Visualization: C. Munteanu, D. C. Turicu, O. Creţ, M. Echim
Writing – original draft: C. Munteanu, D. C. Turicu

Abstract The analysis in real time of space data variability is essential for scientists and space mission controllers. Automated tools designed to extract key descriptors of variability are needed and solutions to adapt such algorithms for on-board computers are rare. This paper describes the design of an automated system for detecting directional discontinuities of a physical quantity and its implementation in Field-Programmable Gate Array (FPGA). The system is currently adapted for solar wind or terrestrial magnetosheath magnetic field directional discontinuities, that is, sharp changes of the magnetic field directionality. Our detection algorithm uses analysis windows of adjustable width and averaging procedures in order to reduce the effects of random fluctuations. A sliding-window approach is designed for continuous monitoring and detection of magnetic directional discontinuities. A software implementation of the algorithm was tested using in-situ magnetic field measurements, and emphasized improvements of performance when using analysis windows of adjustable width. The FPGA implementation of the detection algorithm is built on DILIGENT Nexys 4 DDR featuring a commercial Xilinx Artix-7 device and is designed to be ported to space qualified infrastructure. The FPGA system was tested with synthetic and laboratory signals, and provides results in very good agreement with the software implementation. The FPGA system provides an efficient real-time monitoring solution using minimal computational and energy resources, and reducing the main on-board computer utilization.

1. Introduction

A clear understanding of data variability recorded in space is vital for scientists and space mission controllers. Consequently, automatic tools designed to extract relevant key-descriptors of variability are extremely useful. Nevertheless, solutions to adapt such algorithms for on-board computers are still rare. In this paper we describe an algorithm that detects directional discontinuities of in situ measured variables, and its implementation on Field-Programmable Gate Array (FPGA) devices with an application on directional discontinuities of the interplanetary magnetic field (IMF).

The abrupt changes in the orientation of the IMF, referred to as directional discontinuities (DDs), are known to trigger geomagnetic storms and substorms, with significant impact on ground-based and spaceborne technologies (e.g., Tsurutani et al., 2011, and references therein). DDs are important when estimating the solar wind propagation time from an upstream solar wind monitor to a downstream target (e.g., Haaland et al., 2010; Mailyan et al., 2008; Munteanu et al., 2013). IMF discontinuities play a key role in understanding the micro-scale structure of the solar wind and have been shown to be associated with energetic particle acceleration (e.g., Bandyopadhya et al., 2020; Tessein et al., 2013), and plasma heating (e.g., Osman et al., 2012; Qudsi et al., 2020). With an average occurrence rate of one or two per hour, IMF discontinuities are abundant structures in the solar wind (e.g., Newman et al., 2020) and represent an omnipresent source of variability for the terrestrial plasma environment.

Two general classes of idealized Magnetohydrodynamic (MHD) discontinuities can be distinguished: stationary structures, that is, discontinuities that do not propagate with respect to the ambient plasma (tangential discontinuities (TDs) and contact discontinuities), and propagating discontinuities (rotational discontinuities (RDs) and shocks). The most frequent small-scale discontinuities in the interplanetary space are the abrupt changes in the direction of the magnetic field, predominantly expected for TDs and RDs (e.g., Paschmann et al., 2013).

Two main classes of algorithms to detect solar wind discontinuities are proposed in the literature. The first class includes algorithms searching for changes in the magnetic field direction (Borovsky, 2008, 2010; Burlaga, 1969; Lepping & Behannon, 1986; Li, 2008; Miao et al., 2011; Perri et al., 2012; Zhdankin, Boldyrev, & Mason, 2012; Zhdankin, Boldyrev, Mason, Perez, 2012); the second class includes algorithms searching for

Writing – review & editing: C. Munteanu, D. C. Turicu, O. Creţ, M. Echim

changes in the amplitudes of the magnetic field components and/or magnitude (Greco & Perry, 2014; Greco et al., 2008, 2016, 2018; Sorriso-Valvo et al., 2018; Tsurutani & Smith, 1979; Vasquez et al., 2007).

The term "directional discontinuity" was originally introduced by Burlaga (1969) to denote a variation of solar wind magnetic field direction larger than 30° in less than 30 s. Since then, this definition was used in many variant algorithms. Li (2008) developed an algorithm to identify discontinuities based on this definition. Borovsky (2010) studied the spectral effects of solar wind DDs detected using the definition above. Chian and Muñoz (2011) used the Li (2008) detection method to study the relation between discontinuities, turbulence, and magnetic reconnections at the leading edge of an interplanetary coronal mass ejection. Miao et al. (2011) further developed the algorithm by Li (2008) and introduced a way of determining the discontinuity thickness.

Vasquez et al. (2007) developed an original detection algorithm which is independent of the directional changes, but relies on changes in the amplitude of the magnetic field components. They found that the daily occurrence rate of strong solar wind discontinuities obtained with their original detection algorithm is comparable with the daily occurrence rate obtained using an algorithm based on directional changes. Tsurutani and Smith (1979) also showed that the method used by Burlaga (1969) provides similar results to their method based on changes of the amplitude of field components. Burkholder and Otto (2019) describe yet another original detection algorithm based on changes of the amplitude of field components.

Due to various computational difficulties encountered when implementing automated detection methods, even very recent studies still use visual inspection to identify discontinuities (Artemyev, Angelopouls, & Vasko, 2019; Artemyev, Angelopouls, Vasko, Runov, et al., 2019; Artemyev et al., 2018; Mailyan et al., 2008; Munteanu et al., 2013). Note that the automated detection algorithm of Burkholder and Otto (2019) still uses visual inspection to eliminate events that are not isolated from other structures in the time series. For datasets of only a few hundred events/discontinuities, the detection by visual inspection can be an acceptable option, but, for large-scale statistical studies, visual inspection-based methods are certainly not suitable.

In this study we designed and implemented an original algorithm based on the principles described by Li (2008) (see also Borovsky, 2008). We adopt a discontinuity detection algorithm based on directional changes because: (a) traditionally, angular changes were the preferred detection method (Burlaga, 1969), which renders our approach compatible with previous ones, (b) many authors have recently started to use angular changes in order to improve results from algorithms based on amplitude changes of the field components (e.g., Greco et al., 2018), (c) it is an efficient and less complex approach, thus computationally less intensive and hence less power consuming compared to most algorithms based on amplitude changes of the field components. Since we aim to provide a hardware implementation of our algorithm, the directional changes approach leads to a more reliable and robust FPGA implementation. (d) In many cases, the two approaches are equivalent, especially for discontinuities with rotation angles larger than 30° (e.g., Greco et al., 2018).

State of the art space plasma instruments on-board recent terrestrial or interplanetary missions, for example, MMS (Burch et al., 2016) and Parker Solar Probe (Fox et al., 2016), provide high time-resolution in-situ measurements, while being constrained by limited telemetry possibilities. Thus, the on-board implementation of computations is critical for taking advantage of the full set of collected data. The on-board discontinuity detector would allow for the computation of magnetic field rotation angles from high-resolution measurements without downloading the entire data set. The on-board computed angular changes can also be used to identify interesting events and activate triggers for temporary on-board storage and subsequent download of high-resolution data (selective downlink).

Most of the algorithms discussed above are capable of automatically detecting IMF directional discontinuities, but they were designed only for on-ground data analysis. To our knowledge, no other algorithm was designed to be implemented in an FPGA device. This study is part of a broader effort devoted to building a complex semi-autonomous digital signal processing library, able to apply on-board various digital signal processing techniques. The current version of the library already includes modules devoted for the spectral and statistical analysis of fluctuations (Deak et al., 2018, 2021; Opincariu et al., 2019; Turicu et al., 2022). Here we discuss a new feature, allowing to detect directional discontinuities.

The paper is structured as follows. Section 2 provides a theoretical background and a conceptual description of the discontinuity detection algorithm. It also discusses reconfigurable FPGA devices in the context of on-board data processing. Section 3 gives an overview of the system and describes the FPGA implementation of the discontinuity detection algorithm. Section 4 presents the main tests and validation procedures of both the algorithm and its FPGA implementation; the section shows results obtained using synthetic datasets, laboratory magnetic field measurements, and also in-situ interplanetary magnetic field measurements. Section 5 provides a summary and perspective.

2. Theoretical Background

2.1. Directional Discontinuity Detection Algorithm for Automatic Use

Let us consider a set of in-situ measurements of a plasma or field variable. Take, for instance, the triaxial measurements of the interplanetary magnetic field, B_x, B_y, and B_z, in an arbitrary reference system. Magnetic directional discontinuities observed in interplanetary space and in the terrestrial magnetosheath are characterized by sharp changes in the direction of the magnetic field vector $\boldsymbol{B} = \left[B_x\ B_y\ B_z\right]$. Magnetic directional changes are computed as:

$$\varphi(t_k) = \left(\frac{180}{\pi}\right)\cos^{-1}\left(\frac{\boldsymbol{B}_1 \cdot \boldsymbol{B}_2}{|\boldsymbol{B}_1| \cdot |\boldsymbol{B}_2|}\right) \tag{1}$$

where φ (in degrees) is computed at time t_k, and $\boldsymbol{B}_1$ and $\boldsymbol{B}_2$ are defined as:

$$\begin{aligned} \boldsymbol{B}_1 &= \langle \boldsymbol{B} \rangle_{\tau_1} = \left\langle \left[B_x\ B_y\ B_z\right] \right\rangle_{\tau_1} \\ \boldsymbol{B}_2 &= \langle \boldsymbol{B} \rangle_{\tau_2} = \left\langle \left[B_x\ B_y\ B_z\right] \right\rangle_{\tau_2} \end{aligned} \tag{2}$$

with the symbol $\langle\cdot\rangle_\tau$ denoting time averaging. A window W centered at time t_k is defined: $W = \left[t_{k-l/2},\ t_{k+l/2}\right]$, with l denoting the length of this window. Within this window, the two averaging intervals in Equation 2 are defined as: $\tau_1 = \left[t_{k-l/2},\ t_k\right]$ and $\tau_2 = \left[t_k,\ t_{k+l/2}\right]$. Clearly, τ_1 and τ_2 contain the same number of data samples ($\tau_1 = \tau_2 = l/2$), thus, for brevity, we will refer to either one of these two intervals as TAU. According to Equation 1, φ takes values between 0° (parallel orientation) and 180° (antiparallel orientation).

Other authors used similar definitions for $\boldsymbol{B}_1$ and $\boldsymbol{B}_2$ (e.g., Borovsky, 2008, 2010). Li (2008) and Miao et al. (2011) used only the instantaneous vector measurements at the two edges of the window W. Mailyan et al. (2008) (see also Munteanu et al., 2013) used two time intervals: one for computing the averages, and an additional time interval for separating $\boldsymbol{B}_1$ from $\boldsymbol{B}_2$. For the purpose of this study, we will use $\boldsymbol{B}_1$ and $\boldsymbol{B}_2$ as defined by Equation 2.

Figure 1a depicts a synthetic data set with three components of 1,000 data samples each. The x and y components include sharp discontinuities added onto a constant signal with superposed white Gaussian noise; the z-component is white noise. Figure 1b shows the result obtained with Equation 1 for a window W of 128 data samples centered on the discontinuity. Figure 1b also shows an illustration of the time intervals τ_1 and τ_2 from Equation 2. The two sharp changes in the x and y components correspond, as expected from geometrical considerations, to an angular change of $\varphi \cong 90°$.

For the analysis of a real signal, continuously collected in situ, we developed a sliding-window algorithm which computes the angular changes for windows W centered at each time instance t_k. An illustrative example is shown in Figure 1c. The algorithm starts with the analysis of the first 128 samples of the signal and computes the value $\varphi(t_{64})$ corresponding to the center of this first instance of the analysis window. In the next step the window is moved by one sample, and the procedure is repeated to compute the value $\varphi(t_{65})$. The algorithm continues until the last value $\varphi(t_{936})$ is computed. Figure 1c shows that φ takes values close to 0°up to sample number 436, then it starts to increase as the window position approaches the discontinuity, reaching a maximum value of $\varphi \cong 90°$ at the discontinuity center (at sample 500); then it starts to decrease back toward $\varphi \cong 0°$ (at sample 564). This increasing (decreasing) trend of angular changes is due to the relative position of the sliding window with respect to the actual position of the discontinuity, resulting in amplitude changes as the window moves closer to (away from) the discontinuity. Figure 1 was generated using the software analysis tool Integrated Nonlinear Analysis (INA) (INA, 2016; Munteanu, 2017).

10.1029/2022EA002537

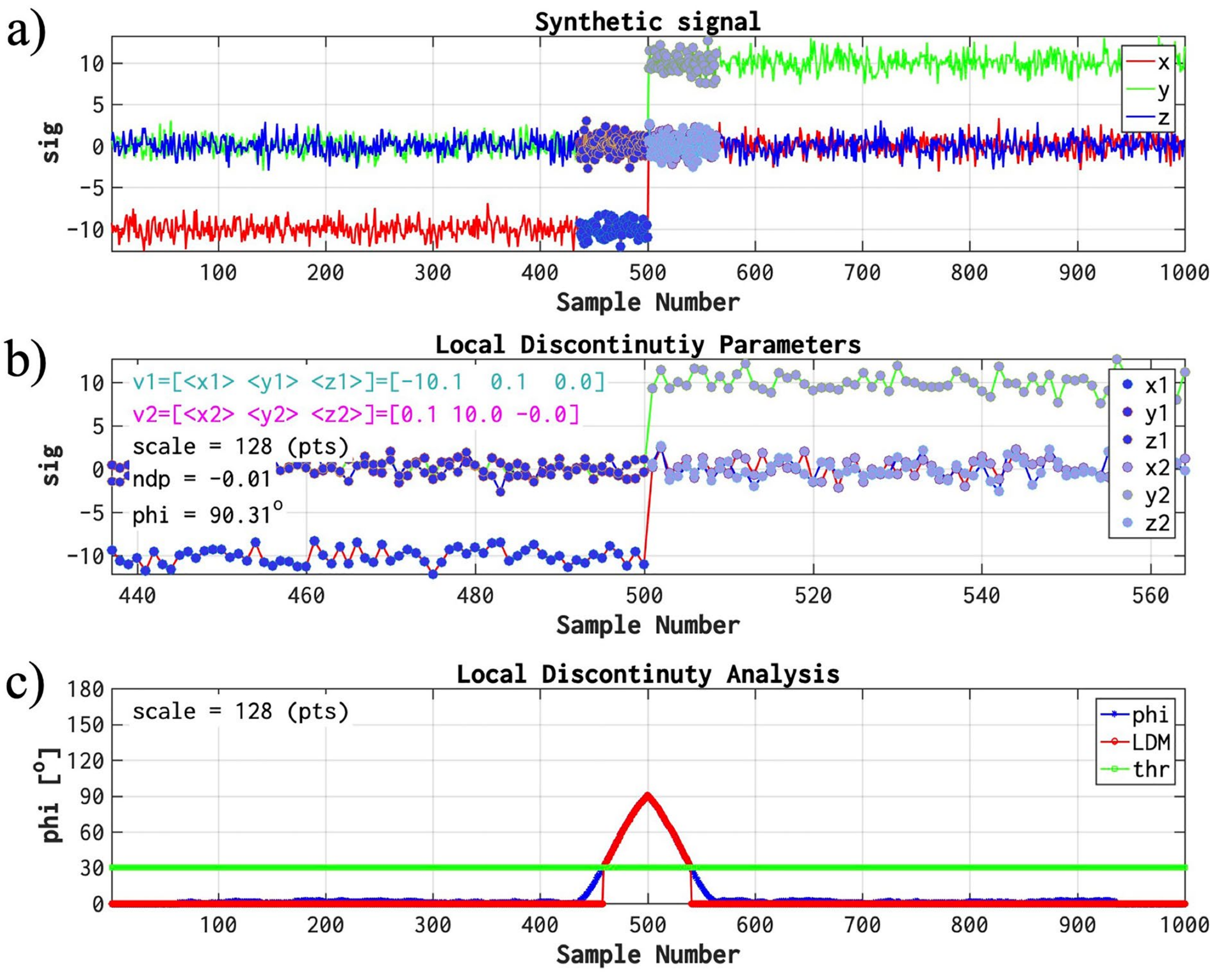

Figure 1. (a) Synthetic data set with three components of 1,000 data samples each. (b) Zoom-in on the 128-sample interval highlighted in the top panel; τ_1 and τ_2 are marked in dark-blue and light-blue, respectively. (c) Local discontinuity analysis of the synthetic data set depicted in panel (a), using a sliding-window of 128 data samples: $\varphi(t_k)$ (from Equation 1; blue line labeled "phi"), local discontinuity measure $\mathrm{LDM}^{(\mathrm{deg})}$ (from Equation 3; red line) and $\varphi_c = 30°$ (green line labeled "thr"). This figure, and also Figures 3–5, were generated using the integrated nonlinear analysis (INA) library (INA, 2016; Munteanu, 2017).

The discontinuity detection algorithm we propose here is based on a critical value of the angular change. This value, denoted in the following as φ_c, is set to 30°. We define a local discontinuity measure (LDM) which is equal to the value of the rotation angle φ, if this is larger than φ_c, and zero otherwise:

$$\mathrm{LDM}^{(\mathrm{deg})}(t_k) = \begin{cases} \varphi(t_k), & \text{if } \varphi(t_k) \geq \varphi_c \\ 0, & \text{otherwise} \end{cases} \tag{3}$$

$\mathrm{LDM}^{(\mathrm{deg})}$ is used as a quantitative measure for the presence of directional discontinuities. Figure 1c shows the $\mathrm{LDM}^{(\mathrm{deg})}$ values computed using Equation 3 for the synthetic signal. As expected, $\mathrm{LDM}^{(\mathrm{deg})}$ is different from zero (and exactly equal to φ) only when $\varphi \geq 30°$.

For an on-board FPGA implementation of the sliding-window algorithm described above, there is no need to apply the $\cos^{-1}$ function and multiply by $(180/\pi)$, as in Equation 1. If needed, these operations can be later performed on ground, using calibrated results. Thus, a simplified version of the method can be implemented in the FPGA device, based solely on the normalized dot product (ndp):

$$ndp\,(t_k) = \frac{\boldsymbol{B}_1 \cdot \boldsymbol{B}_2}{|\boldsymbol{B}_1| \cdot |\boldsymbol{B}_2|} \tag{4}$$

with $\boldsymbol{B}_1$ and $\boldsymbol{B}_2$ defined by Equation 2. From Equations 1 and 4, it follows that angular changes of 180° and 0°, correspond to normalized dot product values of -1 and $+1$, respectively. Similarly, the value of $ndp = 0$ will correspond to an angular change of $\varphi = 90°$. For future reference, the threshold value $\varphi_c = 30°$, corresponds to $ndp_c \cong 0.87$.

Based on the ndp parameter given in Equation 4, a new localized discontinuity measure can be defined:

$$\mathrm{LDM}^{(ndp)}(t_k) = \begin{cases} ndp(t_k), & \text{if } ndp(t_k) \leq ndp_c \\ 0, & \text{otherwise} \end{cases} \tag{5}$$

$\mathrm{LDM}^{(ndp)}$ will be further used in the FPGA implementation of the detection algorithm.

2.2. Reconfigurable FPGA Devices for On-Board Processing

The FPGA devices are integrated circuits containing a matrix of various types of blocks (e.g., configurable logic, memory, digital signal processing, input-output) connected by programmable interconnects. The FPGA devices can be reconfigured to desired functionality.

Modern architectures designed for on-board analysis of data make use of reconfigurable FPGA technology (French et al., 2018; Hanafi et al., 2017; Huber et al., 2007; Kuwahara, 2009; Pingree, 2010), which allows reusing a digital chip via partial or complete reconfiguration. In space, the electronic systems are prone to failures caused by radiations generated by high-energy particles. The FPGA devices are even more vulnerable since radiations can affect their configuration logic and applications data. To mitigate the effect of radiations, specific software and hardware techniques are used for space-qualified FPGA designs (Kalomoiris et al., 2019; Rust et al., 2020). The radiation tolerant FPGA devices from Xilinx (Kintex, 2020; Virtex, 2014, 2018) or Microsemi (Microsemi, 2015) mitigate the effect of space radiations and eliminate the requirement of using dedicated mitigation techniques, like TMR (triple modular redundancy). Our current design/prototype relies on commercial FPGAs and can be ported to radiation hardened architectures (Lee, 2017).

The development flow for FPGA devices is based on a register transfer level (RTL) design methodology. In RTL design, a circuit is described as a set of registers and a set of operations that are performed on the data stored in the registers, using a hardware description language. The high-level synthesis (HLS) technology simplifies the digital signal processing algorithms implementation in FPGA devices allowing the description of the algorithm's functionality using a classical programming language and the generation of the RTL description (Huang et al., 2020; Lahti et al., 2019).

We used HLS to generate an RTL description for the discontinuity detector and an RTL description for the rest of the system components.

3. System Overview and Implementation

The spacecraft's main on-board computers execute multiple critical tasks. Our prototype demonstrates that some tasks can be retargeted to be executed on FPGA devices even at instrument level, thus reducing the main on-board computers' utilization and saving energy resources.

The functionality of the system was validated with synthetic signals, and also with real measurements received from a magnetic sensor, as discussed below. The laboratory tests were performed by continuously monitoring the measurements received from the magnetic sensor and calculating the local discontinuity measures. The output of the system can be used to notify the on-board computer to perform additional analyses or to confirm a status quo in the evolution of the field parameters.

3.1. System Implementation

The directional discontinuity detector based on a local discontinuity measure defined by the Equation 4 is implemented on an affordable Digilent Nexys 4 DDR development board featuring a commercial Xilinx Artix-7 FPGA

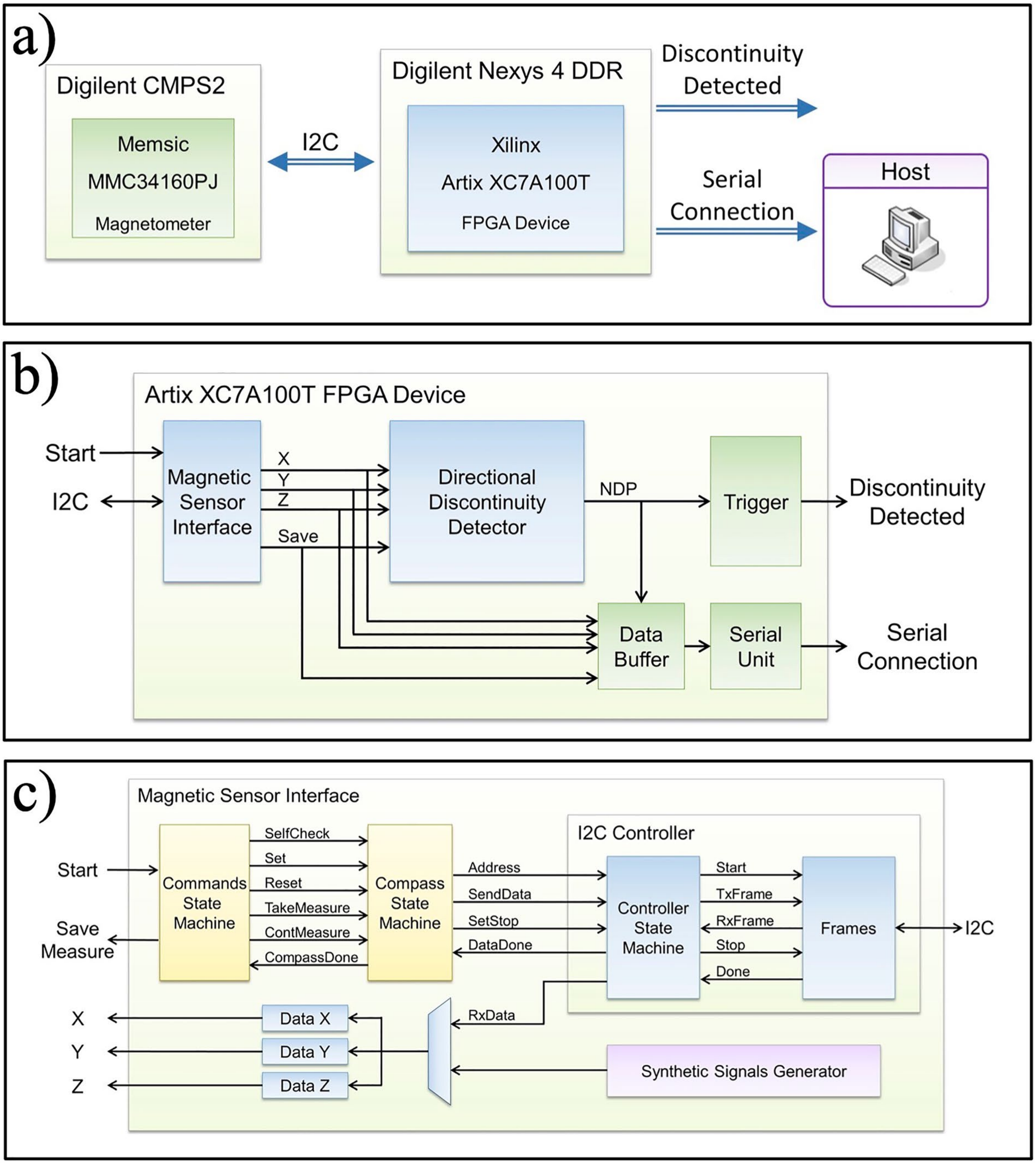

Figure 2. (a) System block diagram. (b) Field-Programmable Gate Array (FPGA) system architecture. (c) Magnetic sensor interface architecture.

device. The Nexys 4 DDR board is a generic development platform with many types of peripherals that can be used for a wide range of designs.

The architecture of the system, shown in Figure 2a, includes a Digilent CMPS2 module attached to the development board to measure the magnetic field. The laboratory prototype includes its own data provider which is a Memsic MMC34160PJ magnetic sensor (www.memsic.com/magnetometer-4) able to perform measurements of the magnetic field on three axes within the full-scale range of ±16 Gauss. The sensor can perform measurements every 10 ms when the resolution of the analog-to-digital convertor is set to 16 bits. The magnetic sensor provides an *I2C* communication channel for configuration, control and to read the measurements.

The discontinuity detector that implements our proposed detection algorithm is implemented in the Xilinx Artix-7 FPGA device. When directional discontinuities are detected, the *Discontinuity Detected* output notifies the main on-board computer or other instruments; this notification can be used to perform, for instance, additional analyses. The *Serial Connection* with the host computer is used only for the validation of the results produced by the system. In a production setup for the system to be deployed on the satellite's on-board FPGA device, the *Serial Connection* will be removed or replaced with other communication protocols to receive the measurements from the on-board magnetic instrument and the computed discontinuity measures.

3.2. FPGA System Design

The design implemented in the FPGA device provides the following functionalities: an *I2C* communication unit to interface with the attached data provider (magnetic sensor), the *Directional Discontinuity Detector* component that analyses the measurements received from the sensor and calculates the discontinuity measures, an *Output* component that notifies the main on-board computer when discontinuities are detected, a *Data Buffer* that aggregates the magnetic sensor measurements and the computed discontinuity measures, and a *Serial Unit* to interface with the host computer for the validation of the system. The architecture of the FPGA design is shown in Figure 2b.

3.2.1. Magnetic Sensor Interface

The *magnetic sensor interface* implements the communication protocol with the Memsic magnetic sensor. The implementation is based on an *I2C* controller which provides a generic implementation of the protocol, and on additional custom circuits to configure and control the magnetic sensor.

Figure 2c shows the architecture of the *magnetic sensor interface*. The *Commands State Machine* and *Compass State Machine* components implement the operations specific to the Memsic magnetic sensor according to the sensor datasheet (www.memsic.com/magnetometer-4), for example, take one measurement, activate continuous measurement mode, and calibration specific commands. The interface also includes the *Synthetic Signals Generator* that generates synthetic signals for the validation of the discontinuity detector.

The communication with the magnetic sensor is initiated by the assertion of the *Start* input signal. A sequence of commands is sent to configure and control the sensor: (a) execute the self-check test, (b) measure and save the calibration offsets, and (c) activate continuous measure mode. After the initial self-check test, the sensor performs two measurements to determine the calibration offsets. Once the calibration phase is finished, the continuous measurements mode is activated and the sensor performs measurements of the three axes every 12 ms. The measurements for each axis are returned on the *X*, *Y*, and *Z* outputs.

3.2.2. Directional Discontinuity Detector

The *Directional Discontinuity Detector* was implemented in C++ and its corresponding RTL description was generated using the high-level synthesis tool from Xilinx. Since the current design assumes a sampling rate of the magnetic sensor of 100 Hz, which is reasonable for on-board triaxial fluxgate magnetometers and is also very low compared to the 100 MHz clock signal driving the FPGA device, the goal set for the high-level synthesis process is to reduce the amount of programmable logic resources required for the design (e.g., Huang et al., 2020; Lahti et al., 2019). Note however that the sampling rate is an adjustable parameter of the system.

The raw measurements received from the magnetic sensor are first converted to Gauss and then passed to the Directional Discontinuity Detector. The pseudocode for the C++ implementation of the detector is depicted in Algorithm 1. The WX, WY, and WZ parameters store the last measurements received from the magnetic sensor. These parameters are implemented as buffers in which each new measurement is saved and the oldest measurement is discarded. The first loop, lines 2–5, computes the sum of the TAU measurements defined by Equation 2 up to the point for which the discontinuity measure defined by Equation 1 is computed. Lines 6–8 calculate the components of the B1 vector as the mean of all these measurements. The second loop, lines 10–13, computes the sum of the TAU measurements received after the point for which the discontinuity measure is computed, and similarly lines 14–16 calculate the components of the B2 vector as the mean of these measurements (see definitions in Equation 2). Line 17 computes the scalar product between the vectors B1 and B2, while lines 18 and 19 compute the norm for each vector. Finally, line 20 computes the discontinuity measure *ndp* defined by Equation 4.

Algorithm 1. Pseudocode for the C++ Implementation of the Discontinuity Detector

```
function Discontinuity_Detector(WX, WY, WZ, TAU):
sum_X ← 0, sum_Y ← 0, sum_Z ← 0
for i = 1 to TAU do
    sum_X ← sum_X + WX[i]
    sum_Y ← sum_Y + WY[i]
    sum_Z ← sum_Z + WZ[i]
B1_X ← sum_X / TAU
B1_Y ← sum_Y / TAU
B1_Z ← sum_Z / TAU
sum_X ← 0, sum_Y ← 0, sum_Z ← 0
for i = TAU to 2*TAU do
    sum_X ← sum_X + WX[i]
    sum_Y ← sum_Y + WY[i]
    sum_Z ← sum_Z + WZ[i]
B2_X ← sum_X / TAU
B2_Y ← sum_Y / TAU
B2_Z ← sum_Z / TAU
product ← B1_X * B2_X + B1_Y * B2_Y + B1_Z * B2_Z
norm_B1 ← SQRT(B1_X*B1_X + B1_Y*B1_Y + B1_Z*B1_Z)
norm_B2 ← SQRT(B2_X*B2_X + B2_Y*B2_Y + B2_Z*B2_Z)
NDP ← product / (norm_B1 * norm_B2)
return NDP
```

3.2.3. Trigger Component and Serial Unit

The *Trigger* component of the FPGA system generates the output of the discontinuity detection system for the main on-board computer or other instruments. The discontinuity measures *ndp* computed by the discontinuity detector are compared against a predefined threshold value. If the value exceeds the threshold defined by Equation 5, the output is asserted to notify the main on-board computer or other devices. Based on the requirements of the on-board computer, the *Trigger* component can be further customized. While this component generates the main output of the system, the *Serial Unit* sends the measurements received from the magnetic sensor and the computed discontinuity measures to a host computer for the validation of the system and visualization of the results.

4. Experimental Results

4.1. Computer Validation of the Discontinuity Detection Algorithm

4.1.1. Testing the Effects of Discontinuity Strength, Signal-To-Noise Ratio, Discontinuity Thickness and Analysis Window Width

We define the "strength" of a directional discontinuity as the amplitude of the angular change across the discontinuity (see Equation 1). Figure 3a shows the results of the LDM algorithm applied on a synthetic three-component vector data set comprised of 3,600 data samples per component. Abrupt amplitude changes in the x and y components are included such that they correspond to angular changes of $\varphi = 180°$ (at sample number 900), $\varphi = 90°$

10.1029/2022EA002537

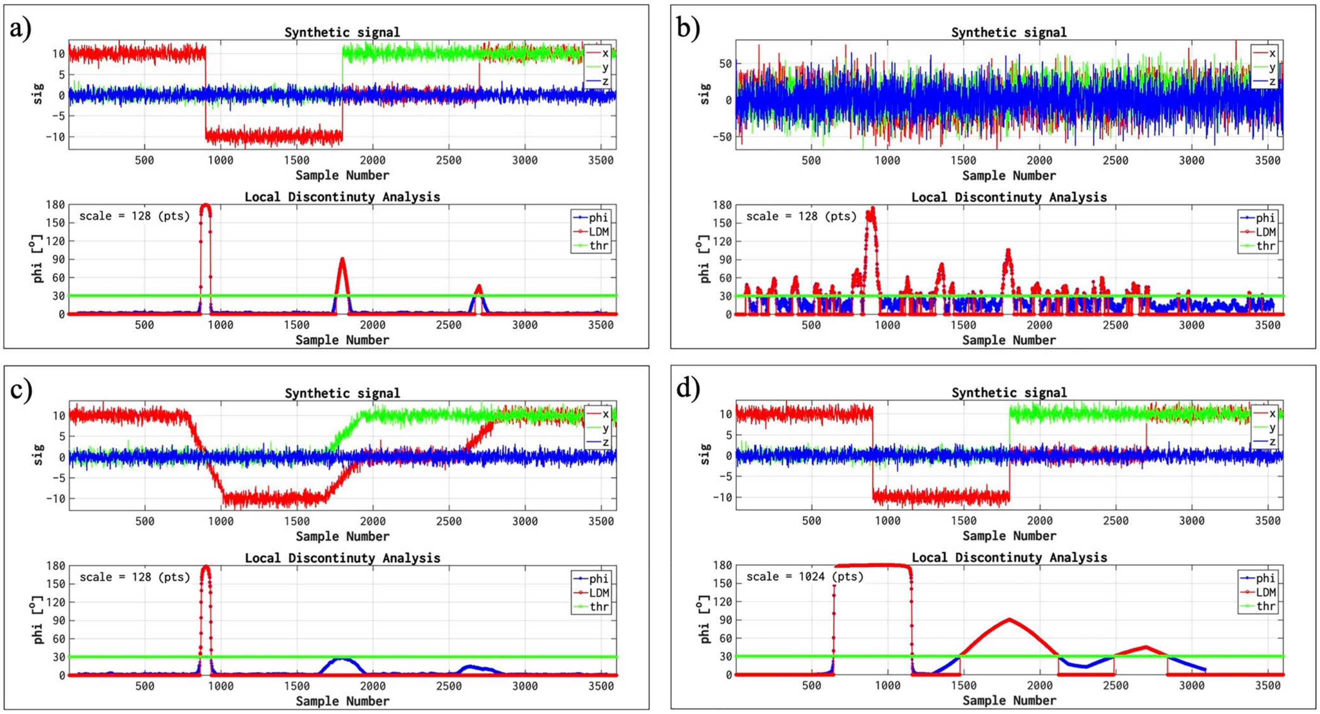

Figure 3. (a) Effect of discontinuity strength. (b) Effect of poor signal-to-noise ratio. (c) Effect of discontinuity width. (d) Effect of window length. In each panel, top plots depict synthetic datasets with three components of 3,600 samples each, and bottom plots depict the local discontinuity analysis using the setup in Figure 1c. Amplitude changes are introduced in all synthetic datasets so as to correspond to angular changes of 180° (at sample number 900), 90° (at 1,800) and 45° (at 2,700). Panels (a) and (d) depict the results for a low noise-level and abrupt (1 sample) amplitude changes, in panel (b) the noise level is increased, and in panel (c) the amplitude changes are widened to span 256 samples each. Local discontinuity analysis is performed using windows of 128 samples (panels a, b, and c) and 1,024 samples (panel d).

(at sample 1,800) and $\varphi = 45°$ (at sample 2,700). The LDM algorithm uses a window W of width $l = 128$ data samples, in this case.

Figure 3a demonstrates that the three predefined angular changes are accurately detected by our proposed discontinuity detection algorithm. Figure 3a shows how the temporal profile of angular changes depends on discontinuity strength. For an angular change of $\varphi = 45°$, one can observe a rather slow increase (decrease) of $\varphi(t_k)$ as we approach (move away from) the center of the discontinuity. For $\varphi = 90°$, the increasing and decreasing trends are faster compared to the $\varphi = 45°$ case. At $\varphi = 180°$ these increasing and decreasing trends almost break down, and we see rather abrupt jumps from $\varphi \cong 0°$ to $\varphi \cong 180°$. These results were obtained for a signal with a small-amplitude white noise whose standard deviation is equal to 0.1.

Figure 3b shows the results of our LDM algorithm when the noise level is increased by adding a white Gaussian noise with a standard deviation equal to 20. Note that the signal amplitude jumps are of 20 units (for $\varphi = 180°$) and 10 units (for $\varphi = 90°$ and $\varphi = 45°$). Figure 3b demonstrates that a high noise level, with standard deviation of the order of the signal amplitude jumps, can easily generate spurious discontinuities above the threshold level of $\varphi_c = 30°$.

Figure 3c illustrates the performance of the LDM algorithm applied on a signal including discontinuities with larger width. This figure demonstrates that when a small analysis window is applied on signals containing thick discontinuities, the algorithm fails to accurately detect discontinuities.

Figure 3d depicts the effect of enlarging the length of the analysis window. In this case the resulting temporal profiles of $\varphi(t_k)$ are much wider around each discontinuity, compared to those in Figure 3a. When the length of the analysis window is comparable to the distance between two adjacent discontinuities, as is the case here, the detection profiles corresponding to each individual discontinuity start to merge and become indistinguishable from each other. By enlarging the analysis window even more, the algorithm will eventually detect only one broad discontinuity. Figure 3d shows results for an analysis window spanning 1,024 samples, which is slightly larger than the separation distance of 900 samples between adjacent discontinuities. One can observe that the discontinuities characterized by angular changes of 90° and 45° are almost fully merged, and undistinguishable by the LDM algorithm.

4.1.2. Improving Detection Accuracy of the LDM Algorithm

Figures 3b–3d identified cases when the discontinuity detection algorithm failed to work properly for one of the following reasons: (a) due to poor signal-to-noise ratio (Figure 3b), (b) due to discontinuities being thicker than the analysis window (Figure 3c), and (c) due to the analysis window being larger that the time interval between adjacent discontinuities (Figure 3d). In this section we discuss how to address these issues and improve the detection accuracy of the algorithm.

When the signal-to-noise ratio is decreased, the accuracy of the LDM algorithm can be maintained by computing the angular changes defined in Equation 1 using a larger number of samples. This can be explained using the standard error of the mean (SEM), a commonly used statistical measure for the differences between the mean value of a sample data set and the mean value of the population from which the sample was drawn. By definition SEM is directly proportional to the standard deviation of the sample data set and inversely proportional to the square root of the sample length. Thus, using a smaller data set length increases SEM, and this increases the statistical uncertainty of the average values used in computing the angular changes. This is even more important in case of poor signal-to-noise ratio, where the larger standard deviation of the data set increases the statistical uncertainty (decreases the statistical significance) of the averages even more. Increasing the width of the analysis window adds more data samples to the analysis and, assuming that no other strong discontinuities are added within this enlarged analysis window, leads to an increased accuracy.

When the width of the analysis window is smaller than the discontinuity thickness, our algorithm computes angular changes using samples only from inside the discontinuity. Thus, assuming that the discontinuity has a simple ramp-like structure (as in Figure 3c), the angular changes computed using small windows will always be smaller than the angular changes computed using windows covering the full width of the discontinuity. As in the previous case, increasing the width of the analysis window will increase the accuracy, assuming again that no other discontinuities are included in the enlarged analysis window.

When more than one discontinuity is present inside the analysis window, we are in a case similar to that depicted in Figure 3d, where the discontinuity detection algorithm fails because the analysis window is wider that the time interval between adjacent discontinuities. In this case, accuracy can be increased by decreasing the width of the analysis window.

Figure 4 illustrates an example on how to improve the algorithm's accuracy by using a larger analysis window. The signal includes three wide discontinuities identical to those in Figure 3c, with the addition of a white Gaussian noise with standard deviation equal to 20, as in Figure 3b. It is shown that increasing the width of the window allows the detection of discontinuities that are missed by shorter windows.

To conclude, a compromise has to be made between enlarging the analysis window in order to increase detection accuracy for wider discontinuities and for those buried in noise, and keeping the analysis window small enough so as to be capable of distinguishing between two adjacent discontinuities separated by a small time-interval.

4.1.3. Computer Validation of the LDM Algorithm Using Interplanetary Magnetic Field Measurements

In the study by Munteanu et al. (2013) we compiled a database consisting of 365 solar wind discontinuities, identified as clear magnetic field rotations by visually examining interplanetary magnetic field measurements. We select a sample from that database, consisting of magnetic field measurements (at 16 s time resolution) from the Advanced Composition Explorer (ACE) spacecraft in 06 January 2003. Figure 5 illustrates the results of the discontinuity detection algorithm applied on these real-life, in-situ measurements.

Several specific features are observed in Figure 5. Let us examine the discontinuity around sample 3,250. As we increase the window width, the LDM profile corresponding to this discontinuity becomes wider, as expected. In this case, the peak value of $\varphi(t_k)$ computed by our algorithm remains almost unchanged as we increase the width of the analysis window: the discontinuity amplitude is slightly above 100° for the first two windows, and slightly below 100° for the last two windows. The situation is very different for the discontinuity centered around sample

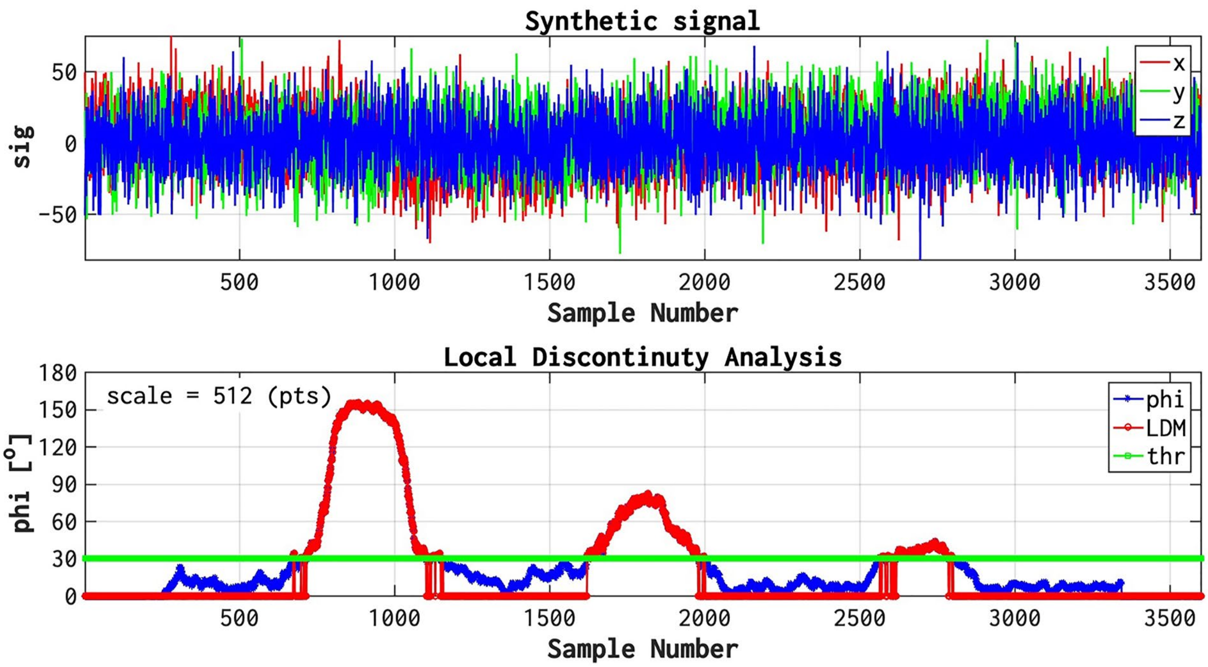

Figure 4. Example on how to mitigate the effects of increased noise-level and discontinuity thickness, by using larger windows. Top plot: synthetic data containing three 256-samples-wide discontinuities superposed onto white Gaussian noise with standard deviation equal to 20 units. Bottom plot: local discontinuity analysis with windows of 512 samples, depicted using the setup in Figure 1c.

4,000. In this latter case, $\varphi(t_k)$ decreases systematically, from a value around 120° for the window whose length is set to 32 samples, to a value of 60° for the window whose length is equal to 256 samples.

Other features can also be observed in Figure 5. The first part of the series, up to sample number 2000, shows very different scaling properties in terms of the number of discontinuities, compared to the second part of the series. The smallest window detects the largest number of discontinuities, and, as we increase the width of the analysis window, more and more discontinuities that are close to each other start to merge. See for example, the part of the signal centered around sample 1,500. Three distinct discontinuities are detected by the 32-samples analysis window. Using a 64-samples window, the weakest discontinuity starts to merge with the middle amplitude one. Using 128-samples, only two discontinuities are detected, and both are much weaker compared to the strongest one detected using the 32-samples window. The 256-samples window detects only one weak discontinuity around sample number 1500.

The results described above, are similar to the results discussed by Greco et al. (2016). They also observed complex "break ups" and "ramifications" going from singular large-scale discontinuities to multiple small-scale ones, giving rise to a tangled network of primary and secondary structures. We retrieve same types of structures in our LDM results obtained for the group of discontinuities observed around sample 1,500 of the signal depicted in Figure 5.

4.2. Implementing the Discontinuity Detector in FPGA

The initial prototype of the directional discontinuity detection algorithm was implemented in INA (Munteanu, 2017), a MATLAB-based software analysis tool. The algorithm was tested with series of signals that highlight different kinds of discontinuities, as described in Section 4.1.

For the FPGA implementation of the detection system, we used high-level synthesis to generate the RTL implementation of the discontinuity detection algorithm as described by Equations 2–5. Since the Xilinx Vivado HLS 2019.1 (Vivado, 2019b) does not support MATLAB as programming language for the description of the algorithms, the discontinuity detection algorithm was first rewritten in C++.

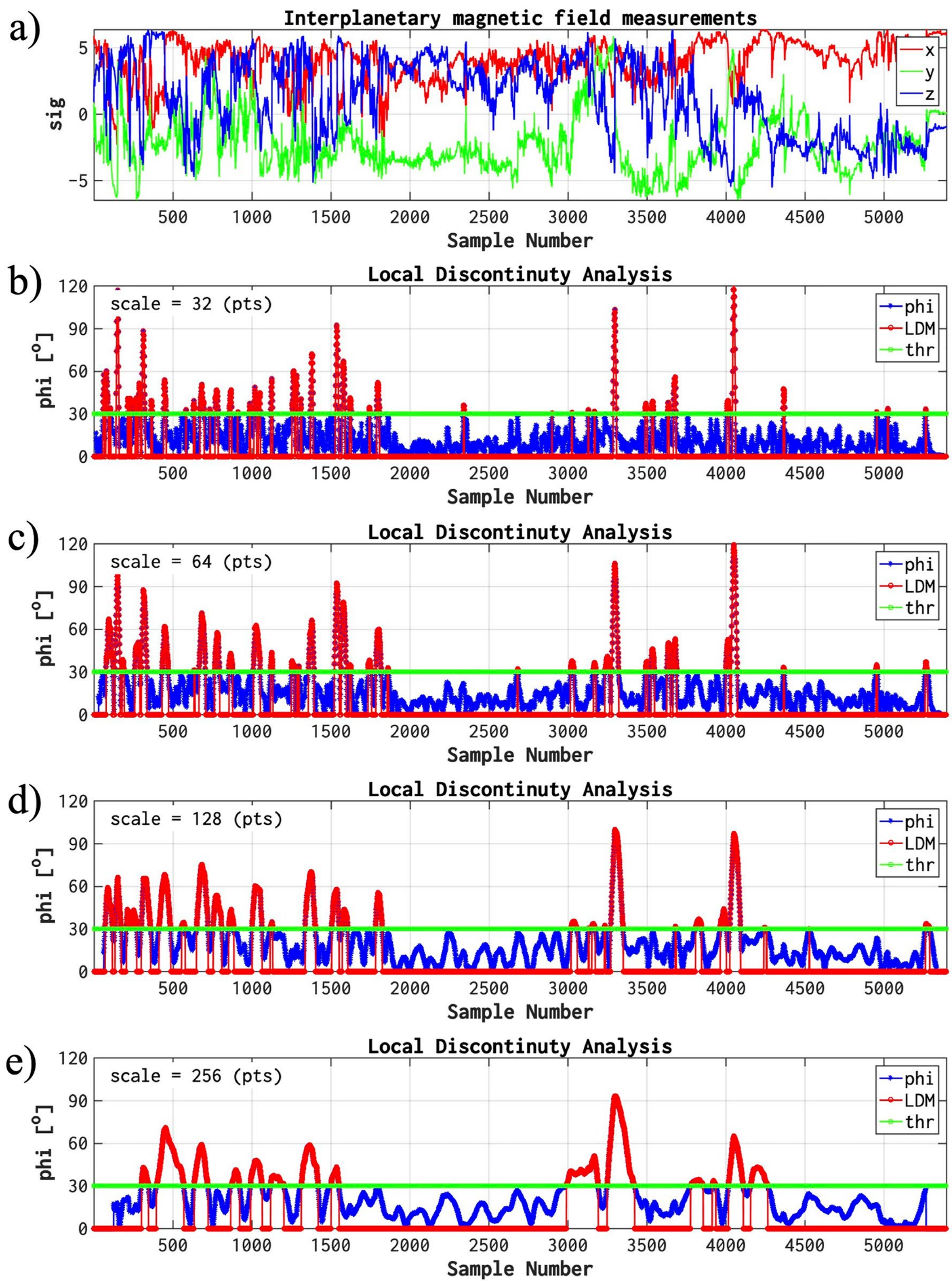

Figure 5. Computer validation of the directional discontinuity detector using interplanetary magnetic field (IMF) measurements from the Advanced Composition Explorer (ACE) spacecraft in 06 January 2003. (a) IMF components as function of sample number. (b–e) Local discontinuity analysis: $\varphi(t_k)$ (from Equation 1; blue line labeled "phi"), $\mathrm{LDM}^{(\mathrm{deg})}$ (from Equation 3; red line) and $\varphi_c = 30°$ (green line labeled "thr"). The panels depict results using windows of 32 samples (panel b), 64 (panel c), 128 (panel d), and 256 samples (panel e), respectively.

Table 1
Analyzed Data Types and Resulting Errors

Test signal	Data type	Max error	Errors count
Synthetic	Float	0.000000	0
Capture	Float	0.000000	0
Synthetic	Half	0.756262	90
Capture	Half	0.302604	3,976
Synthetic	FXP<32,16>	1.984288	7,402
Capture	FXP<32,16>	1.818750	4,259
Synthetic	FXP<32,14>	1.999315	593
Capture	FXP<32,14>	1.967990	4,235
Synthetic	FXP<32,20>	0.017650	4
Capture	FXP<32,20>	0.998943	5,588
Synthetic	FXP<32,22>	0.170812	10
Capture	FXP<32,22>	1.435630	5,910

To validate the C++ implementation of the algorithm, we designed and implemented a testbench in Vivado HLS which generates the series of synthetic signals and the series of measurements captured by the magnetic sensor as inputs for the discontinuity detector, and then compares the results with the ones generated by the MATLAB prototype for the same inputs.

4.2.1. Data Types Analysis

The Xilinx Vivado HLS provides support for all the standard C++ datatypes and also supports additional data types which can generate more efficient hardware implementations for the algorithms. Several data types were analyzed for the implementation of the discontinuity detector. The algorithm uses advanced mathematical functions which are supported by the Vivado HLS math library.

Table 1 shows the analyzed data types and the computed errors between the results generated by the MATLAB implementation and the results of the C++ implementation for the series of synthetic signals described in Figure 6a, and the measurements captured by the magnetic sensor described in Figure 6b. The *Max Error* column describes the maximum absolute difference between the discontinuity measures computed by the MATLAB and the C++ implementations for the same series of inputs. The *Errors Count* column reports the number of absolute differences which are higher than 0.001, an arbitrarily selected threshold. Based on these results, we selected the float data type (single-precision) for the implementation of the discontinuity detector as it provides a good trade-off between precision and efficiency of the hardware implementation.

4.2.2. Discontinuity Detector Analyses

The Xilinx Vivado HLS allows a direct inference of the RTL component from the C++ source code, thus ensuring a high-quality implementation in the FPGA device. In order to improve the quality of the generated RTL implementation, several code optimizations were analyzed and evaluated after circuit synthesis, based on the timing and resource utilization estimates provided by the Xilinx Vivado HLS tool.

These optimizations were not automatically generated but had to be developed by the research team. In the final version of the discontinuity detection algorithm we replaced the regular C++ arrays which store the last received measurements with shift registers. The sums of the measurements in buffers are maintained in variables which are adjusted for every new measurement received by adding the value of the new measurement and subtracting the value of the measurement leaving the buffer. This way, we eliminate the algorithm loops (see Algorithm 1) which compute the sums of the measurements in buffers.

Table 2 describes the timing estimates for the implementation of the discontinuity detector with different values for the TAU parameter. The implementation targets a clock period of 10 ns, due to the 100 MHz oscillator present on the development board which clocks the FPGA device. This timing constraint is met for all tested values of the TAU parameter.

The *Initiation Interval* defines the minimum and maximum number of clock cycles before new measurements can be accepted, while the *Latency* specifies the minimum and maximum number of clock cycles required to compute the discontinuity measure *ndp* (see Equation 5). Considering that we configured the magnetic sensor to take a new measure every 12 ms, these requirements are also satisfied. Also, the results show that with the shift registers optimization the timing parameters are not influenced by the size of the TAU parameter.

Table 2 also describes the estimated programmable logic resources required for the implementation of the discontinuity detector in the FPGA device with different values for the TAU parameter. The results show that the TAU parameter influences the required number of Block-RAM resources of the FPGA device, while the amount of the other programmable logic resources remains constant.

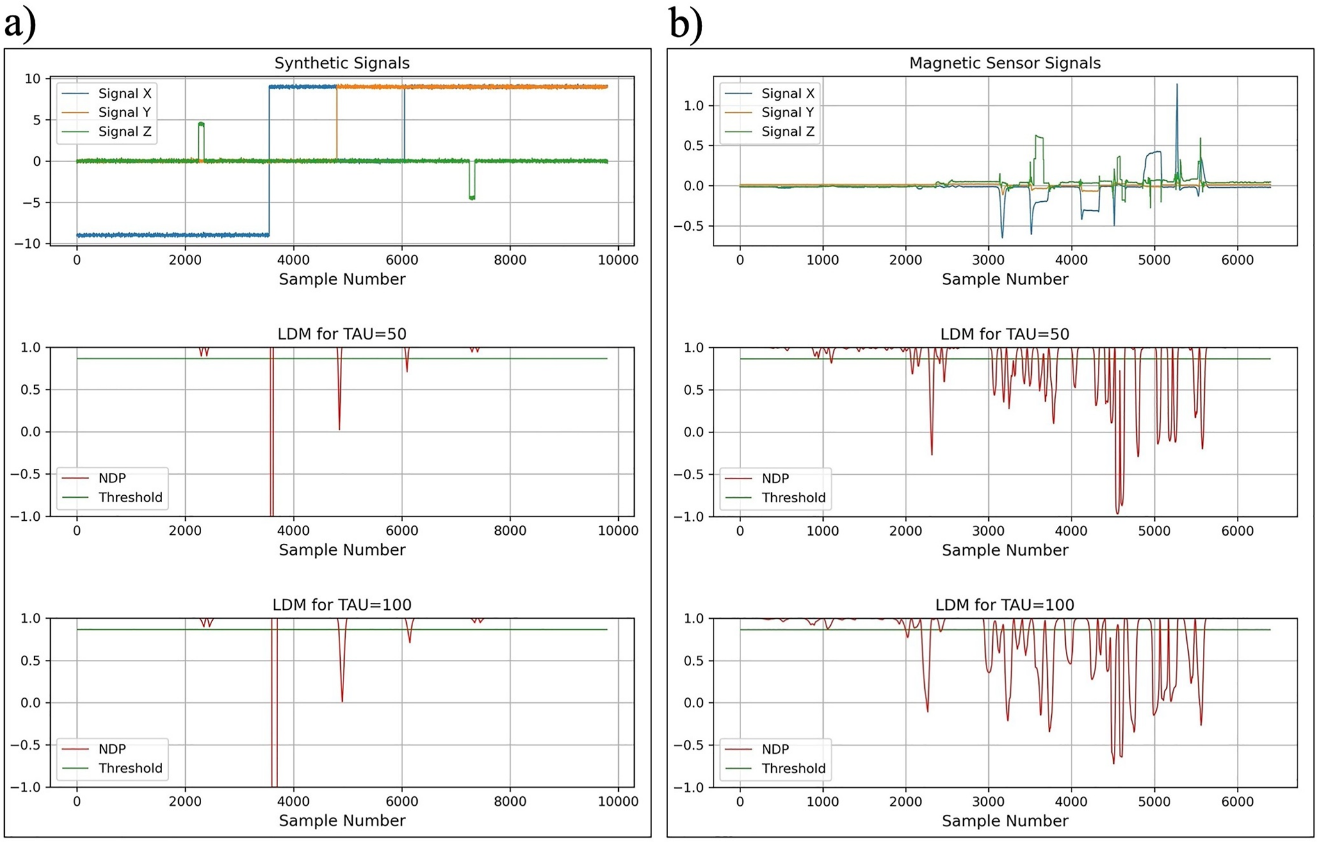

Figure 6. Validation of the discontinuity detector in Field-Programmable Gate Array (FPGA) using: (a) synthetic signals, and (b) measurements received from the magnetic sensor. In both panels, top plot shows the analyzed data set; middle plot depicts *ndp* (from Equation 4; red line) for TAU = 50 samples; the *ndp* threshold (green line) is at $ndp_c \cong 0.87$; bottom plot, same as middle plot, but for TAU = 100 samples.

The discontinuity detectors for two arbitrarily selected values of the TAU parameter, 50 and 100, were generated and exported from Vivado HLS to be integrated with the rest of the system components (see Section 3.2) for validation.

4.3. Validation of the Discontinuity Detector in FPGA

The RTL description of the discontinuity detector generated by the Xilinx Vivado HLS was integrated with rest of the system as described in Section 3. The system implemented in the Artix-7 FPGA device using the Xilinx

Table 2
Vivado HLS Timing and Utilization Estimates for the Discontinuity Detector

	Timing estimates						Utilization estimates			
	Clock		Initiation interval		Latency					
	Target	Estimated	Clock cycles		Clock cycles					
TAU samples	ns	ns	min	max	min	max	BRAM	DSP	FF	LUT
50	10	9.384	74	88	74	88	0	24	7,562	7,949
100	10	9.384	74	88	74	88	0	24	7,562	7,949
500	10	9.384	74	88	74	88	6	24	7,400	7,577
1,000	10	9.384	74	88	74	88	12	24	7,403	7,577
5,000	10	9.384	74	88	74	88	96	24	7,412	7,580

Vivado 2019.1 (Vivado, 2019a) suite was tested with synthetic signals and real measurements of the magnetic field received from the magnetic sensor.

The measurements and the computed discontinuity measures *ndp* are sent to the host machine for visualization and the results were compared with the ones obtained with the MATLAB implementation (adapted according to Equation 4). The maximum absolute error between the two implementations is 0.

Figure 6a shows the local discontinuity measures computed using FPGA for three synthetic signals with 10,000 samples each. Note that the threshold value between weak and strong discontinuities used in the MATLAB-based results from Section 4.1, that is, $\varphi_c = 30°$, corresponds to a normalized dot product value of $ndp_c \cong 0.87$ (see Section 2.1). Also note the thresholding of φ stated that all angular changes larger 30° corresponded to strong discontinuities. In the case of the *ndp* parameter (defined in Equation 4) the situation is somewhat different: all normalized dot product values in the interval [0.87, 1] are "below" the threshold value, and are considered weak discontinuities, while *ndp* values in the interval [−1, 0.87], are "above" the threshold, and correspond to strong discontinuities.

Figure 6a demonstrates that the *ndp* measure is capable of accurately detecting all directional discontinuities included in the synthetic data set. In particular, three strong discontinuities dominate the results: the first one around sample 3,500, with ndp = −1, that is, $\varphi = 180°$ (see Equations 1 and 4); the second one around sample 5,000, with $ndp = 0$, that is, $\varphi = 90°$; and the third one around sample 6,000, with $ndp \cong 0.71$, that is, $\varphi = 45°$. These strong discontinuities are all accurately detected "above" the threshold value (see the previous paragraph).

The synthetic data set of Figure 6a also includes a few additional weak discontinuities: a set of two around sample 2,500 and another set around sample 7,500. One can observe that the *ndp* measure is able to detect even these weak discontinuities, but, since they are "below" the threshold value, they will not activate the *Trigger Component* of the FPGA system (see Section 3.2.3).

Another noteworthy result in Figure 6a is the fact that all directional discontinuities detected by the FPGA device, even the weakest ones, show a persistency of the value of the *ndp* measure as we increase the analysis window from TAU = 50 to TAU = 100 samples. This is consistent with the results illustrated in Figures 3a and 3d (see also Figure 5), and is due to the fact that all discontinuities in Figure 6a are isolated structures, that is, the time intervals between adjacent discontinuities are larger than the width of the analyzing window. This is not the case for the signal in Figure 6b, as we describe next.

Figure 6b shows the results obtained for measurements received from the magnetic sensor. To artificially modify the magnetic field measured by the sensor, a magnet was used to produce the sharp variations observed in the measured magnetic field. Figure 6b demonstrates that the *ndp* measure computed by the FPGA device is capable of accurately detecting directional discontinuities even for these highly fluctuating measurements received from the magnetic sensor. One can observe that multiple weak discontinuities are detected using the small analysis window (TAU = 50 samples), but some of them are not detected as distinct events when the larger analysis window (TAU = 100 samples) is used. This is because the weaker discontinuities have merged into a single profile (similar to the case around sample 1,500 in Figure 5). A clear example can be seen around sample 2,500: for TAU = 50 samples, two relatively weak discontinuities with *ndp* values slightly above the threshold limit are observed; for TAU = 100, only one of these two discontinuities is detected, with a corresponding value for the *ndp* measure equal to the threshold limit.

Other interesting features evidenced by Figure 6b are the large changes of the peak *ndp* values as we change the width of the analysis window. This is due to the fact that adjacent discontinuities are separated mostly by time intervals which are smaller than the width of the analysis window. See, for example, the two strongest discontinuities around sample 4,500: for TAU = 50 samples, they have *ndp* values slightly below −1, that is, $\varphi \cong 180°$; while for TAU = 100, their *ndp* values are only slightly "above" − 0.5, that is, $\varphi \cong 120°$.

4.4. Energy Efficiency and Device Utilization

Table 3 describes the type and the amount of FPGA device reconfigurable resources used by the implementation of the whole system in an Artix XC7A100T-CSG324 FPGA device for the selected values of the TAU parameter,

Table 3
FPGA Device Resource Utilization

	Utilization			Utilization %	
Resource	TAU 50	TAU 100	Available	TAU 50	TAU 100
LUT	7,110	7,491	63,400	11.21	11.82
LUTRAM	522	809	19,000	2.75	4.26
FF	6,165	6,165	126,800	4.86	4.86
BRAM	3	3	135	2.22	2.22
DSP	24	24	240	10.00	10.00

50 and 100 samples. These results, generated after implementation, show that the system uses just a small part of the FPGA device resources, allowing for other functionalities to be implemented in the same device.

We also computed power estimates for the whole system implemented in the FPGA device. Our device power analysis showed that, from a total On-Chip Power of 0.261 W (100%), the Device Static Power was 0.098 W (37%) and the Dynamic Power was 0.163 W (63%). The power analysis for the design was performed using the default environmental settings in Xilinx Vivado 2019.1 environment.

5. Summary and Conclusions

We designed an algorithm to continuously compute changes in the direction of a three-component vector quantity. The algorithm was first implemented in the MATLAB-based software tool Integrated Nonlinear Analysis—INA (INA, 2016; Munteanu, 2017). This software implementation was used for the validation and testing of the algorithm for various synthetic datasets and in-situ magnetic field measurements. The algorithm's functionality is demonstrated for magnetic discontinuities in space, but, due to its adjustable parameters, the detection method can be used to analyze any vector quantity for which rapid direction changes are important.

In space physics, the term "directional discontinuity" was originally used to denote a change in interplanetary magnetic field (IMF) direction of more than 30° in less than 30 s. The exact threshold between weak and strong discontinuities and also their duration can vary significantly depending on the specific datasets being used and/or specific science questions being addressed. Random fluctuations in the direction of the IMF are ubiquitous, due to either natural variability and/or instrumental noise, making it almost impossible to use such fixed threshold values (e.g., 30 sec. for duration, or 30° for strength). Our algorithm uses adjustable thresholds, adjustable widths for the analysis windows and also averaging procedures in order to reduce the adverse effects of the background variability on the detection accuracy. A sliding-window algorithm is also designed in order to perform real-time monitoring and continuous discontinuity detection.

The directional discontinuity detection algorithm is adapted for and implemented on a FPGA device. In order to optimize the FPGA implementation, the complex calculations of angular changes used by the software implementation, which required the use of trigonometric functions, were replaced by much simpler calculations based solely on dot products, which require only basic arithmetic operations.

The FPGA design was extensively validated and tested using multiple synthetic datasets and real-life laboratory magnetometer measurements. Detailed experimental results regarding energy efficiency, power consumption, and resource utilization demonstrate the usefulness of the design and the feasibility of an FPGA-based discontinuity detector for a real-time monitoring of observables on-board spacecraft.

We also report the optimizations applied on the FPGA design in order to minimize the computational resources and ensure an efficient utilization of the limited computational and energy resources available on-board. The simplicity of the design flow, the flexibility and the short time to market of the FPGA devices, can constitute a pathway for future data analysis strategies.

The discontinuity detection algorithm described in this paper is part of a broader effort meant to build an integrated library for autonomous on-board digital signal processing. This library already includes modules designed for spectral and statistical analysis of on-board data and is able to produce a set of key data descriptors when the entire data stream cannot be sent to the ground for further analysis.

Data Availability Statement

In Section 4.1.3 we tested the directional discontinuity detector using magnetic field data from the MAG instrument (Smith et al., 1998) on-board the Advanced Composition Explorer (ACE) spacecraft. We analyzed a 24-hr time interval, at 16 s time resolution, covering the whole day of 06 January 2003. The ACE-MAG Level 2 data

(ACE-MAG, 2022) are publicly available at: https://izw1.caltech.edu/ACE/ASC/level2/lvl2DATA_MAG.html. Figures 1 and 3–5, were generated using the Integrated Nonlinear Analysis (INA) library (INA, 2016; Munteanu, 2017). The INA software is publicly available for download from the STORM-FP7 project website at: http://www.storm-fp7.eu/index.php/data-analysis-tools.

Acknowledgments

This work was supported by the Romanian Ministry of Research and Innovation via PCCDI Grant 18PCCDI/2018 and National Core Program (LAPLAS 2019). The work of M.E. was supported by ESA PRODEX CLUSTER (PEA4000130552) and Belgian Solar Terrestrial Center of Excellence (STCE). The work of C.M. was supported by projects PN-III-P1-1.1-TE-2019-1288 and PN-III-P1-1.1-TE-2021-0102 and ESA PRODEX MISION (PEA4000134960).

References

ACE-MAG (2022). Level 2 data from the magnetic field experiment (MAG) onboard the advanced composition explorer (ACE) spacecraft. Interplanetary Magnetic Field Data, [Dataset]. https://izw1.caltech.edu/ACE/ASC/level2/lvl2DATA_MAG.html

Artemyev, A. V., Angelopoulos, V., Halekas, J. S., Vinogradov, A. A., Vasko, I. Y., & Zelenyi, L. M. (2018). Dynamics of intense currents in the solar wind. *The Astrophysical Journal*, *859*(2), 95. https://doi.org/10.3847/1538-4357/aabe89

Artemyev, A. V., Angelopoulos, V., & Vasko, I. Y. (2019). Kinetic properties of solar wind discontinuities at 1 AU observed by ARTEMIS. *Journal of Geophysical Research: Space Physics*, *124*(6), 3858–3870. https://doi.org/10.1029/2019JA026597

Artemyev, A. V., Angelopoulos, V., Vasko, I. Y., Runov, A., Avanov, L. A., Giles, B. L., et al. (2019). On the kinetic nature of solar wind discontinuities. *Geophysical Research Letters*, *46*(3), 1185–1194. https://doi.org/10.1029/2018GL079906

Bandyopadhyay, R., Matthaeus, W. H., Parashar, T. N., Chhiber, R., Ruffolo, D., Goldstein, M. L., et al. (2020). Observations of energetic-particle population enhancements along intermittent structures near the sun from the parker solar probe. *The Astrophysical Journal Supplement Series*, *246*(2), 61. https://doi.org/10.3847/1538-4365/ab6220

Borovsky, J. E. (2008). Flux tube texture of the solar wind: Strands of the magnetic carpet at 1 AU? *Journal of Geophysical Research: Space Physics*, *113*(A8), A08110. https://doi.org/10.1029/2007JA012684

Borovsky, J. E. (2010). Contribution of strong discontinuities to the power spectrum of the solar wind. *Physical Review Letters*, *105*(11), 111102. https://doi.org/10.1103/PhysRevLett.105.111102

Burch, J. L., Moore, T. E., Torbert, R. B., & Giles, B. L. (2016). Magnetospheric multiscale overview and science objectives. *Space Science Reviews*, *199*(1–4), 5–21. https://doi.org/10.1007/s11214-015-0164-9

Burkholder, B. L., & Otto, A. (2019). Magnetic reconnection of solar flux tubes and coronal reconnection signatures in the solar wind at 1 AU. *Journal of Geophysical Research: Space Physics*, *124*(11), 8227–8254. https://doi.org/10.1029/2019JA027114

Burlaga, L. F. (1969). Directional discontinuities in the interplanetary magnetic field. *Solar Physics*, *7*(1), 54–71. https://doi.org/10.1007/BF00148406

Chian, A. C.-L., & Muñoz, P. R. (2011). Detection of current sheets and magnetic reconnections at the turbulent leading edge of an interplanetary coronal mass ejection. *The Astrophysical Journal Letters*, *733*(2), L34. https://doi.org/10.1088/2041-8205/733/2/L34

Deak, N., Creţ, O., Echim, M., Teodorescu, E., Negrea, C., Văcariu, L., et al. (2018). Edge computing for space applications: Field programmable gate array-based implementation of multiscale probability distribution functions. *Review of Scientific Instruments*, *89*(12), 125005. https://doi.org/10.1063/1.5044425

Deak, N., Creţ, O., Munteanu, C., Teodorescu, E., & Echim, M. M. (2021). FPGA design for on-board measurement of intermittency from in-situ satellite data. *Earth and Space Science*, *8*(12), e2021EA001678. https://doi.org/10.1029/2021EA001678

Fox, N. J., Velli, M. C., Bale, S. D., Decker, R., Driesman, A., Howard, R. A., et al. (2016). The solar probe plus mission: Humanity's first visit to our star. *Space Science Reviews*, *204*(1–4), 7–48. https://doi.org/10.1007/s11214-015-0211-6

French, M., Schmidt, A. G., Skalicky, S., Flately, T., Crum, G., Geist, A., et al. (2018). *SpaceCubeX2—Heterogeneous on-board processing for distributed measurement and multi-satellite missions*. NASA Earth Science Technology Forum (ESTF). Retrieved from https://www3.isi.edu/people/aschmidt/publications/spacecubex2_heterogeneous_-board_processing_distributed_measurement_and

Greco, A., Chuychai, P., Matthaeus, W. H., Servidio, S., & Dmitruk, P. (2008). Intermittent MHD structures and classical discontinuities. *Geophysical Research Letters*, *35*(19), L19111. https://doi.org/10.1029/2008GL035454

Greco, A., Matthaeus, W. H., Perri, S., Osman, K. T., Servidio, S., Wan, M., & Dmitruk, P. (2018). Partial variance of increments method in solar wind observations and plasma simulations. *Space Science Reviews*, *214*, 1. https://doi.org/10.1007/s11214-017-0435-8

Greco, A., Perri, S., Servidio, S., Yordanova, E., & Veltri, P. (2016). The complex structure of magnetic field discontinuities in the turbulent solar wind. *The Astrophysical Journal Letters*, *823*(2), L39. https://doi.org/10.3847/2041-8205/823/2/L39

Greco, A., & Perry, S. (2014). Identification of high shears and compressive discontinuities in the inner heliosphere. *The Astrophysical Journal*, *784*(2), 163. https://doi.org/10.1088/0004-637X/784/2/163

Haaland, S., Munteanu, C., Mailyan, B., Pulkkinen, & Raststätter, L. (2010). Solar wind propagation delay: Comment on "Minimum variance analysis-based propagation of the solar wind observations: Application to real-time global magnetohydrodynamic simulations" by A. *Space Weather*, *8*(6), S06005. https://doi.org/10.1029/2009SW000542

Hanafi, A., Karim, M., Latachi, I., Rachidi, T., Dahbi, S., & Zouggar, S. (2017). FPGA-based secondary on-board computer system for low-Earth-Orbit Nano-satellite. In *International Conference on Advanced Technologies for Signal and Image Processing (ATSIP)*. https://doi.org/10.1109/ATSIP.2017.8075514

Huang, L., Li, D. L., Wang, K. P., Gao, T., & Tavares, A. (2020). A survey on performance optimization of high-level synthesis tools. *Journal of Computer Science and Technology*, *35*(3), 697–720. https://doi.org/10.1007/s11390-020-9414-8

Huber, F., Behr, P., Röser, H. P., & Pletner, S. (2007). FPGA based on-board computer system for the "flying laptop" micro-satellite. In *Proceedings of DASIA 2007*. European Space Agency.

INA. (2016). An integrated nonlinear analysis (INA) library developed during European Community's seventh framework programme project storm (solar system plasma turbulence: Observations, inteRmittency and multifractals). STORM, [Software]. Retrieved from https://www.storm-fp7.eu

Kalomoiris, I., Pitsis, G., Tsagkatakis, G., Ioannou, A., Kozanitis, C., Dollas, A., et al. (2019). An experimental analysis of the opportunities to use field programmable gate array multiprocessors for on-board satellite deep learning classification of spectroscopic observations from future ESA space missions". In *European workshop on on-board data processing (OBDP2019)*. Retrieved from https://indico.esa.int/event/225

Kintex (2020). RT kintex ultrascale FPGAs for ultra high throughput and high bandwidth applications WP523 (v1.0). Retrieved from https://docs.xilinx.com/v/u/en-US/wp523-xqrku060

Kuwahara, T. (2009). *FPGA-based reconfigurable on-board computing systems for space applications*, Ph.D. Thesis, Institute of Space Systems University at Stuttgart.

Lahti, S., Sjövall, P., Vanne, J., & Hämäläinen, T. D. (2019). Are we there yet? A study on the state of high-level synthesis. *IEEE Transactions on Computer-Aided Design of Integrated Circuits and Systems*, *38*(5), 898–911. https://doi.org/10.1109/TCAD.2018.2834439

Lee, D. S. (2017). Commercial field-programmable gate arrays for space processing applications. In *Commercial Field-Programmable Gate Arrays for Space Processing Applications* conference. Retrieved from https://www.osti.gov/servlets/purl/1458107

Lepping, R. P., & Behannon, K. W. (1986). Magnetic field directional discontinuities: Characteristics between 0.46 and 1.0 AU. *Journal of Geophysical Research*, *91*(A8), 8725–8741. https://doi.org/10.1029/JA091iA08p08725

Li, G. (2008). Identifying current-sheet-like structures in the solar wind. *The Astrophysical Journal*, *672*(1), L65–L68. https://doi.org/10.1086/525847

Mailyan, B., Munteanu, C., & Haaland, S. (2008). What is the best method to calculate the solar wind propagation delay? *Annals of Geophysics*, *26*(8), 2383–2394. https://doi.org/10.5194/angeo-26-2383-2008

Miao, B., Peng, B., & Li, G. (2011). Current sheets from Ulysses observation. *Annals of Geophysics*, *29*(2), 237–249. https://doi.org/10.5194/angeo-29-237-2011

Microsemi (2015). Mitigation of radiation effects in RTG4 radiation-tolerant flash FPGAs (2015) WP0191 white paper. Retrieved from https://www.microsemi.com/document-portal/doc_download/135027-wp0191-mitigation-of-radiation-effects-in-rtg4-radiation-tolerant-fpgas-white-paper

Munteanu, C. (2017). *Turbulent fluctuations and discontinuities in the solar wind: Statistical properties and possible effects on the terrestrial plasma environment*, Ph.D. Thesis, Faculty of Physics, Doctoral School of Physics, University of Bucharest, Romania. Retrieved from https://gpsm.spacescience.ro/gpsm/core/doc/publicatii/teze/Costel_Munteanu_UniBuc_thesis_final_version.pdf

Munteanu, C., Haaland, S., Mailyan, B., Echim, M., & Mursula, K. (2013). Propagation delay of solar wind discontinuities: Comparing different methods and evaluating the effect of wavelet denoising. *Journal of Geophysical Research: Space Physics*, *118*(7), 3985–3994. https://doi.org/10.1002/jgra.50429

Newman, R., Vainchtein, D., & Artemyev, A. (2020). Solar wind transient currents: Statistical properties and impact on Earth's magnetosphere. *Solar Physics*, *295*(9), 129. https://doi.org/10.1007/s11207-020-01695-z

Opincariu, L., Deak, N., Creţ, O., Echim, M., Munteanu, C., & Văcariu, L. (2019). Edge computing in space: Field programmable gate array-based solutions for spectral and probabilistic analysis of time series. *Review of Scientific Instruments*, *90*(11), 114501. https://doi.org/10.1063/1.5119231

Osman, K. T., Matthaeus, W. H., Wan, M., & Rappazzo, A. F. (2012). Intermittency and local heating in the solar wind. *Physical Review Letters*, *108*(26), 261102. https://doi.org/10.1103/PhysRevLett.108.261102

Paschmann, G., Haaland, S., Sonnerup, B., & Knetter, T. (2013). Discontinuities and Alfvénic fluctuations in the solar wind. *Annals of Geophysics*, *31*(5), 871–887. https://doi.org/10.5194/angeo-31-871-2013

Perri, S., Goldstein, M. L., Dorelli, J. C., & Sahraoui, F. (2012). Detection of small-scale structures in the dissipation regime of solar-wind turbulence. *Physical Review Letters*, *109*, 19. https://doi.org/10.1103/PhysRevLett.109.191101

Pingree, P. J. (2010). Advancing NASA's on-board processing capabilities with reconfigurable FPGA technologies: Opportunities and implications. In *IEEE international symposium on parallel distributed processing, workshops, and PhD forum (IPDPSW)*. https://doi.org/10.1109/IPDPSW.2010.5470824

Qudsi, R. A., Maruca, B. A., Matthaeus, W. H., Parashar, T. N., Bandyopadhyay, R., Chhiber, R., et al. (2020). Observations of heating along intermittent structures in the inner heliosphere from PSP data. *The Astrophysical Journal Supplement Series*, *246*(2), 46. https://doi.org/10.3847/1538-4365/ab5c19

Rust, J., Hao, M., Karsthof, L., Paul, S., Hashem, E., & Kulau, U. (2020). A high-performance data processing unit for next generation satellite transceivers. *IEEE International Conference on Wireless for Space and Extreme Environments (WiSEE)*, 35–38. https://doi.org/10.1109/WiSEE44079.2020.9262643

Smith, C. W., L'Heureux, J., Ness, N. F., Acuña, M. H., Burlaga, L. F., & Scheifele, J. (1998). The ACE magnetic fields experiment. *Space Science Reviews*, *86*(1/4), 613–632. https://doi.org/10.1023/A:1005092216668

Sorriso-Valvo, L., Perrone, D., Pezzi, O., Valentini, F., Servidio, S., Zouganelis, I., & Veltri, P. (2018). Local energy transfer rate and kinetic processes: The fate of turbulent energy in two-dimensional hybrid Vlasov–Maxwell numerical simulations. *Journal of Plasma Physics*, *84*(2), 725840201. https://doi.org/10.1017/S0022377818000302

Tessein, J. A., Matthaeus, W. H., Wan, M., Osman, K. T., Ruffolo, D., & Giacalone, J. (2013). Association of suprathermal particles with coherent structures and shocks. *The Astrophysical Journal Letters*, *776*(1), L8. https://doi.org/10.1088/2041-8205/776/1/L8

Tsurutani, B. T., Lakhina, G. S., Verkhoglyadova, O. P., Gonzalez, W. D., Echer, E., & Guarnieri, F. L. (2011). A review of interplanetary discontinuities and their geomagnetic effects. *Journal of Atmospheric and Solar-Terrestrial Physics*, *73*(1), 5–19. https://doi.org/10.1016/j.jastp.2010.04.001

Tsurutani, B. T., & Smith, E. J. (1979). Interplanetary discontinuities: Temporal variations and the radial gradient from 1 to 8.5 AU. *Journal of Geophysical Research*, *84*(A6), 2773–2787. https://doi.org/10.1029/JA084iA06p02773

Turicu, D. C., Creţ, O., Echim, M., & Munteanu, C. (2022). An FPGA-based solution for computing a local stationarity measure from satellite data. *IEEE Access*, *10*, 9668–9676. https://doi.org/10.1109/ACCESS.2022.3143239

Vasquez, B. J., Abramenko, V. I., Haggerty, D. K., & Smith, C. W. (2007). Numerous small magnetic field discontinuities of Bartels rotation 2286 and the potential role of Alfvénic turbulence. *Journal of Geophysical Research*, *112*(A11), A11102. https://doi.org/10.1029/2007JA012504

Virtex (2014). Space-grade Virtex-4QV family overview DS653 (v2.1). Retrieved from https://docs.xilinx.com/v/u/en-US/ds653

Virtex (2018). Radiation-hardened, space-grade Virtex-5QV family data sheet: Overview DS192 (v1.6). Retrieved from https://docs.xilinx.com/v/u/en-US/ds192_V5QV_Device_Overview

Vivado (2019a). Vivado design suite user guide 2019.1. Retrieved from https://www.xilinx.com/support/documentation/sw_manuals/xilinx2019_2/ug901-vivado-synthesis.pdf

Vivado (2019b). Vivado high-level synthesis user guide 2019 (p. 1). Retrieved from https://www.xilinx.com/support/documentation/sw_manuals/xilinx2019_1/ug902-vivado-high-level-synthesis.pdf

Zhdankin, V., Boldyrev, S., & Mason, J. (2012). Distribution of magnetic discontinuities in the solar wind and in magnetohydrodynamic turbulence. *The Astrophysical Journal Letters*, *760*, 2. https://doi.org/10.1088/2041-8205/760/2/L22

Zhdankin, V., Boldyrev, S., Mason, J., & Perez, J. C. (2012). Magnetic discontinuities in magnetohydrodynamic turbulence and in the solar wind. *Physical Review Letters*, *108*, 17. https://doi.org/10.1103/PhysRevLett.108.175004